FAP106 is an interaction hub required for stable assembly of conserved and lineage-specific proteins at the cilium inner junction

[a]Michelle M. Shimogawa, [a]Angeline S. Wijono, [a,b,c]Hui Wang, [d]Jihui Sha, [a]Natasha Szombathy, [a]Sabeeca Vadakkan, [a]Paula Pelayo, [a]Keya Jonnalagadda, [d]James Wohlschlegel, [a,c,e]Z. Hong Zhou*, and [a,c,e]Kent L. Hill*

[a]Department of Microbiology, Immunlogy and Molecular Genetics, University of California Los Angeles, Los Angeles, CA, 90095

[b]Department of Bioengineering, University of California Los Angeles, Los Angeles, CA, 90095

[c]California NanoSystems Institute, University of California Los Angeles, Los Angeles, CA, 90095

[d]Department of Biological Chemistry, University of California Los Angeles, Los Angeles, CA, 90095

[e]Molecular Biology Institute, University of California Los Angeles, Los Angeles, CA, 90095

Running title: *T. brucei* MIPs

*Corresponding authors:

Kent L. Hill

609 Charles E. Young Drive E, MSB 1602-G, Los Angeles, CA 90095

kenthill@microbio.ucla.edu

Z. Hong Zhou

CNSI 5511C, 570 Westwood Plaza, Los Angeles, CA 90095

Hong.Zhou@UCLA.edu

Author contributions

Designed research: MS, AW, HW, HZ, KH

Performed research: MS, AW, HW, JS, NS, SV, PP, KJ

Contributed new reagents or analytic tools:

Analyzed data: MS, AW, HW, JS, NS, SV, PP, KJ, JW, HZ, KH

Wrote the paper: MS, AW, HW, HZ, KH

ABSTRACT

Eukaryotic motile cilia/flagella are conserved organelles important for cell propulsion and fluid flow, typically built around a "9+2" axoneme of nine doublet microtubules (DMTs) encircling a central pair of singlet microtubules. The DMT lumen is lined with an interconnected network of microtubule inner proteins (MIPs), some conserved and others lineage-specific. MIPs augment the tubulin lattice of the DMT, directly impacting stability, fine structure, and motility, thus providing an important source of lineage-specific adaptations. *Trypanosoma brucei* is a flagellated eukaryotic pathogen with distinctive motility that is critical for pathogen transmission and pathogenesis. Prior studies revealed lineage-specific *T. brucei* MIPs, but their identities are unknown. To identify *T. brucei* MIPs, we examined flagellum structure and composition following knockdown of FAP106, a conserved MIP at the inner junction (IJ) connecting A- and B-microtubules of the DMT. FAP106 knockdown resulted in short flagella and defective parasite motility, supporting a role for MIPs in *T. brucei* flagellum stability and motility. Cryogenic electron tomography (cryoET) and quantitative proteomics identified several conserved MIPs and lineage-specific MIP structures and MIP candidate proteins (MCs) that depend on FAP106 for stable assembly. We further demonstrate by knockdown and fitting AlphaFold models to cryoET maps that one of these, MC8, is a newly identified lineage-specific MIP required for normal parasite motility. This work provides an important advance toward elucidating the order of assembly of MIPs at the cilium inner junction and identifies trypanosome proteins specific to these deadly pathogens that represent targets to consider for therapeutic intervention.

SIGNIFICANCE STATEMENT

Motility characteristics of cilia/flagella differ dramatically between species to accommodate organism-specific motility needs. Recently discovered microtubule inner proteins (MIPs) inside

microtubules are thought to contribute to species-specific motility characteristics but are largely uncharacterized. The flagellated parasite, *Trypanosoma brucei*, exhibits many unique motility features considered important for moving through host tissues to cause disease, but identities of parasite-specific MIPs are unknown. Here, we combine structural biology, mutant analysis, and quantitative proteomics to identify lineage-specific MIPs in *T. brucei*. We demonstrate that the conserved MIP, FAP106, is required for motility and stable assembly of several other MIPs, including trypanosome-specific MIPs required for motility. Our studies advance fundamental understanding of MIP assembly mechanisms, while identifying parasite-specific proteins as potential targets for therapeutic intervention.

INTRODUCTION

Cilia (synonymous with eukaryotic flagella) are conserved, microtubule-based structures that provide motility and signaling functions at the surface of eukaryotic cells. Cilium motility is required for normal human reproduction, development, physiology, and to combat infection (1). Motile cilia also drive cell propulsion in eukaryotic pathogens responsible for tremendous human suffering worldwide (2, 3). Given this broad distribution and central importance to eukaryote cell biology and human health, understanding structural foundations of cilium assembly and motility is of broad interest.

Most motile cilia are built around a "9 + 2" cylindrical axoneme consisting of nine doublet microtubules (DMTs) surrounding a central pair of singlet microtubules. Each DMT is comprised of a complete, 13-protofilament A-microtubule (A-tubule) and a partial, 10-protofilament B-microtubule (B-tubule), with non-tubulin proteins forming an “inner junction” (IJ) filament that connects the A- and B-tubules (4, 5). Recent studies have revealed a previously unappreciated, yet universal feature of motile axonemes, showing that DMTs are not hollow but, instead, are lined with a highly organized network of interconnected “microtubule inner proteins” (MIPs) (6-

9). Structures inside DMTs had been reported several decades ago in flagellated protozoa (10, 11), but the diversity and ubiquitous distribution of such structures was not recognized until cryogenic electron tomography (cryoET) enabled high-resolution, 3D structural analysis (8, 12). Studies in organisms from diverse eukaryotic lineages (13-16) indicate MIPs are present in both the A- and B-tubules and occur in a regularly repeating pattern along the length of the DMT in all motile axonemes. Their broad taxonomic distribution indicates MIPs are fundamentally important for axoneme function and likely were present prior to eukaryote diversification. Meanwhile absence of regularly spaced MIP structures in non-motile cilia (17, 18) suggests they are required specifically for motile axonemes. Pioneering work in *Chlamydomonas* and *Tetrahymena* demonstrated they can enhance DMT stability and influence beating of the axoneme (19, 20). MIPs have also been shown to affect tubulin dimer packing and protofilament spacing (13, 14, 16), axoneme curvature (14, 20, 21), and outer dynein assembly (13, 16, 22). Nonetheless, many aspects of MIP functions remain poorly understood.

In recent, groundbreaking work, cryogenic electron microscopy (cryoEM) was used to reconstruct near-atomic resolution structures of the axoneme, thereby allowing *in situ* identification and atomic modeling of MIPs in *Chlamydomonas*, *Tetrahymena,* and mammals (13, 16, 21, 23). These studies have expanded opportunities for studying MIP function and revealed that while some MIPs are conserved across diverse taxa, others represent lineage-specific adaptations (13, 16, 21, 23). Axonemes of diverse organisms share general architecture and beating mechanism, and lineage-specific MIPs therefore offer a potential mechanism for meeting organism-specific motility characteristics (2, 15, 24), such as those presented by movement of parasitic protozoa through tissues of their human and animal hosts (25, 26). Identification and analysis of lineage-specific MIPs are therefore of great interest.

African trypanosomes, e.g. *Trypanosoma brucei* and related kinetoplastids, are flagellated, protozoan pathogens that cause extensive human suffering and limit economic

75 development in some of the world's poorest regions (27, 28). Trypanosomes also represent
76 diverse eukaryotic lineages that have proven useful for uncovering novel features of eukaryote
77 biology (29, 30). *T. brucei* motility exhibits several distinctive features that support movement
78 through host tissues (15, 31) and is required for pathogenesis (32) and transmission (33). The
79 *T. brucei* flagellum has a large and diverse repertoire of MIP structures, including several that
80 are lineage-specific, particularly in the B-tubule (15). Except for a few conserved examples,
81 however, proteins comprising most *T. brucei* MIP structures are unknown, representing a critical
82 knowledge gap in *T. brucei* flagellum assembly and motility.

83 We sought to identify *T. brucei* MIPs, with a focus on those that are lineage-specific.
84 Loss of one MIP often compromises additional MIPs (20, 21, 34, 35), and our strategy was
85 therefore to identify proteins altered upon disruption of a known MIP. We selected FAP106, a B-
86 tubule MIP that spans the IJ, interconnects other MIPs in *Chlamydomonas*, *Tetrahymena*, and
87 mammals (13, 16, 21, 35), and may contact several lineage-specific MIP structures in *T. brucei*
88 (15). Requirement of FAP106 for IJ or MIP assembly has not been tested in any organism. By
89 RNAi depletion, we show that *T. brucei* FAP106 is required for parasite motility and normal
90 flagellum length. CryoET and tandem mass tag (TMT) quantitative proteomics together show
91 that FAP106 knockdown (KD) results in loss of conserved IJ MIP structures and their
92 corresponding proteins, as well as additional MIP structures and proteins corresponding to
93 lineage-specific MIP candidates (MCs). One of these candidates, MC8, was confirmed by
94 cryoET to be a novel lineage-specific *T. brucei* MIP and is required for normal motility. Together,
95 our results demonstrate that FAP106 is a critical interaction hub required for stable assembly of
96 conserved and lineage-specific MIPs at the inner junction. This work advances understanding of
97 MIP assembly mechanisms and provides insight into parasite-specific MIPs that control *T.*
98 *brucei* motility. Because they are not present in the mammalian host, such MIPs are attractive
99 for consideration as targets for therapeutic intervention in trypanosome infections.

100 # RESULTS

101 **FAP106 is required for parasite motility.**

102 Of eight B-tubule MIPs identified in *Chlamydomonas* (16), only three have clear homologs in *T.*
103 *brucei*: FAP45, FAP52, and FAP106 (Table 1). The IJ filament proteins, PACRG and FAP20 (4,
104 5), are also conserved. FAP45 and FAP52 sit adjacent to the IJ and are required for DMT
105 stability (16, 19, 21). FAP106 forms a 'tether loop' structure that spans the inner junction and is
106 interconnected with several other MIPs (13, 16, 21, 35), although the requirement for FAP106 in
107 MIP and IJ assembly has not been tested. We used tetracycline-inducible RNAi (36) to deplete
108 FAP106 in procyclic form cells, hereafter referred to as "FAP106 KD". RNAi knockdown reduced
109 FAP106 mRNA expression by more than 95% (Fig. 1A) without affecting parasite growth rate
110 (Fig. 1B). FAP106 KD parasites did not exhibit any gross morphological defects, although their
111 flagella were shorter than normal (Fig. 1C-E). Notably, despite having a beating flagellum,
112 FAP106 KD parasites rarely exhibited directional motility, even at high cell densities, which
113 typically result in faster directional motility (Fig. 1F-G; Supp. Fig. S1). Thus, FAP106 is critical
114 for normal parasite motility.

115 **FAP106 is required for stable assembly of IJ MIPs and other MIP structures.**

116 To determine whether FAP106 is required for assembly of other MIP structures, we performed
117 cryoET on purified, demembranated flagella from control and FAP106 KD parasites. Most
118 known MIPs assemble with a periodicity of 16, or 48 nm (9, 13-16, 21, 23, 35, 37) and we
119 therefore performed subtomogram averaging to determine the 48-nm repeating unit of the DMT
120 (Fig. 2; Supp. Fig. S2; Movie 1) for comparison to the published structures of the 48-nm repeat
121 from other organisms (13, 16, 21). MIP densities in the A-tubule appeared largely unaffected in
122 the FAP106 KD and, given the position of FAP106 in the B-tubule, we focused our analysis on
123 the B-tubule. Cross-sectional views of the cryoET tomogram show several major B-tubule MIP

124 densities are missing in the FAP106 KD. Although we do not have sufficient resolution to
125 identify the corresponding proteins directly, referencing the position of MIPs conserved in other
126 organisms provides insight. Longitudinal and cross-sectional views (Fig. 2C-D; Movie 1) show
127 loss of densities corresponding to the 'tether loop' structure of FAP106 in algae and mammals
128 (13, 16, 21) (Fig. 2B-C, red), consistent with the idea that FAP106 structure is conserved across
129 species (13). A density corresponding to the expected position of FAP52 (16, 19, 21) appears
130 largely unaffected in the FAP106 KD (Fig. 2B-D, tan; Movie 1). We did not resolve filamentous
131 densities corresponding to FAP45 on protofilaments B6-B9 in other organisms (13, 16), but
132 these protofilaments were heavily decorated in *T. brucei* control cells and relatively devoid of
133 MIP densities in FAP106 KD (Fig. 2D; Movie 1). Additionally, densities corresponding to the
134 expected position of the FAP45 N-terminus are reduced in the FAP106 KD (Fig. 2D, orange).
135 Thus, FAP106 appears to be required for proper assembly of FAP45 but not FAP52.
136 Interestingly, the FAP106 KD also shows loss of FAP106-associated densities that resemble
137 FAP210 in other organisms (Fig. 2B, 2D, green; (13, 16, 21, 35)), although *T. brucei* lacks a
138 clear FAP210 homolog (Table 1). Overall, our results indicate FAP106 is critical for stable
139 assembly of a subset of B-tubule MIP structures in the vicinity of the IJ.

140 Beyond known MIP structures defined in other organisms, additional densities reduced
141 in the FAP106 KD correspond to MIP structures that are absent in one or more other organisms.
142 These lineage-specific MIP structures include a protruding density on protofilament B8, "MIP
143 B8", densities attached to protofilament A12, "MIP A12", and a protruding density on
144 protofilament B5, "MIP B5" (Fig. 2B). A density with location and periodicity similar to MIP B8 is
145 present in *Tetrahymena* (9, 23, 35, 37), but not in *Chlamydomonas* or mammals (13, 16). MIP
146 A12 densities (Fig. 2B-C) are not present in *Chlamydomonas* or mammals (13, 16, 21) and
147 appear more prominent in *T. brucei* than MIP5a and MIP5b located at a similar position in
148 *Tetrahymena* (9, 23, 35, 37). A density analogous to MIP B5 is not observed in any other

149 published structures (9, 13, 16, 23, 35, 37). Thus, FAP106 is required for stable assembly of
150 universally-conserved, as well as lineage-specific MIPs.

151 **FAP106 is required for assembly of a subset of PACRG subunits into the IJ filament.**

152 The IJ filament is a conserved non-tubulin structure that connects protofilaments A1 and B10 in
153 organisms with cilia (8, 18). The IJ filament is comprised of PACRG and FAP20 subunits that
154 alternate each 4nm along the axoneme (4, 5). Interestingly, most organisms have a single hole
155 in the IJ filament every 96nm, corresponding to one missing PACRG subunit per 96-nm
156 repeating unit (8, 12, 37). *T. brucei* is unusual in having two holes per 96-nm repeating unit (15)
157 (Fig. 2E). The function of the IJ hole is not known, nor is the structural basis for the presence of
158 two holes per 96nm in *T. brucei*. Strikingly, our cryoET data show that loss of FAP106 results in
159 two additional holes per 48-nm repeat, giving six holes per 96-nm repeat (Fig. 2E). These holes
160 correspond to loss of every fourth subunit of the IJ filament (light blue in Fig. 2E), which, based
161 on analogy with *Chlamydomonas* (16), likely corresponds to PACRG.

162 **TMT proteomics identifies novel, lineage-specific MIPs.**

163 To identify proteins corresponding to FAP106-dependent MIP densities, we used tandem mass
164 tag (TMT) quantitative proteomics to compare the protein composition of purified,
165 demembranated flagella from control and FAP106 KD parasites. We quantified more than 2500
166 proteins and only eight of these were significantly reduced in flagella from FAP106 KD parasites
167 ($\geq$2-fold reduced, adjusted p-value $\leq$0.06) (Fig. 3A; Table 2; Supp. Dataset S1). Three proteins
168 were observed to be increased in the knockdown (Fig. 3A; Supp. Dataset S1) and were not
169 studied further.

170 As expected, the protein most reduced in FAP106 KD parasites was FAP106 itself (Fig.
171 3A; Table 2), confirming efficient knockdown reported by qRT-PCR (Fig. 1A) and loss of
172 FAP106 protein from the axoneme (Fig. 2). Two other characterized proteins, FAP45 and

173 PACRG-B, were also reduced in the FAP106 KD (Fig. 3A-B, Table 2). FAP45 was almost 4-fold
174 reduced in FAP106 KD flagella (Fig. 3A; Table 2), supporting results from cryoET indicating
175 FAP106 is required for stable assembly of FAP45 into the axoneme (Fig. 2). FAP52 and FAP20
176 were unaffected (Supp. Dataset S1), further supporting conclusions from cryoET that these
177 proteins assemble independently of FAP106 (Fig. 2). Notably, *T. brucei* has two PACRG
178 homologs, PACRG-A and PACRG-B (Table 1), which have been suggested to be functionally
179 redundant (38, 39). Despite a high degree of similarity, however, PACRG-A and PACRG-B are
180 readily distinguishable by mass spectrometry and our TMT proteomics analysis shows that only
181 PACRG-B is lost in the FAP106 KD (Fig. 3A; Table 2; Supp. Dataset S1). Loss of PACRG-B
182 and not PACRG-A indicates that the extra holes in the FAP106 KD (Fig. 2E) correspond to
183 missing PACRG-B subunits and demonstrates that PACRG-A and PACRG-B are not redundant.
184 Based on spacing of IJ subunits, the two IJ holes in control parasites most likely also
185 correspond to missing PACRG-B.

186 The identity of proteins corresponding to FAP106-dependent MIP densities that are
187 lineage-specific (Fig. 2) are unknown. In addition to the known MIPs described above, five
188 previously uncharacterized proteins were reduced in flagella from FAP106 KD parasites (Fig.
189 3A; Table 2). One of these proteins (RPC19, Tb927.11.8890) localizes to the nucleus (40),
190 suggesting it is unlikely to be a MIP. The remaining four proteins (Tb927.10.7120,
191 Tb927.11.4920, Tb927.11.2770, and Tb927.3.3200), which are kinetoplastid-specific and
192 localize to the flagellum (Supp. Fig. S3A; (40)), are strong candidates for lineage-specific,
193 FAP106-dependent MIPs. Importantly, these four proteins were also identified as “MIP
194 candidates”, MC3, MC5, MC8, and MC15, in a completely independent APEX2-based proximity
195 proteomics analysis as being nearby FAP45 and FAP52 in the B-tubule (Supp. Fig. S4; Supp.
196 Dataset S2). Identification of these four proteins by independent approaches greatly supports
197 their potential as novel, kinetoplastid-specific MIPs.

198 To test the requirement of MC3, MC5, MC8 and MC15 for flagellum structure and
199 function, we used tetracycline-inducible RNAi to individually knockdown each of these proteins.
200 Knockdown resulted in loss of the respective proteins (Supp. Fig. S3A) without substantial
201 effects on parasite growth. Loss of MC5 did not affect parasite motility, while MC3, MC8, and
202 MC15 are each required for normal motility (Fig. 3C; Supp. Fig. S3B). MC8 KD and MC15 KD
203 parasites also showed small reductions in flagellum length (Fig. 3D; Supp. Fig. S3C). To ask
204 whether additional proteins depend on these MCs for assembly into the axoneme, we
205 performed TMT proteomics on flagella isolated from parasites in which the individual MCs were
206 knocked down (Supp. Fig. S3D-G; Supp. Dataset S1). These proteomic analyses confirm
207 significant reduction of each MC in the respective knockdown, but no additional proteins were
208 lost ($\geq$2-fold reduced, adjusted p-value $\leq$0.06) in any of the four knockdowns (Supp. Fig. S3D-G,
209 Supp. Dataset S1). Therefore, motility defects in MC3, MC8, and MC15 knockdowns reflect a
210 requirement for these individual, kinetoplastid-specific proteins in trypanosome motility.

211 **MC8 is a novel, lineage-specific *T. brucei* MIP that comprises the MIP B8 density.**

212 To identify MIPs corresponding to FAP106-dependent MIP densities, we fit the AlphaFold (41,
213 42) models of the above MCs into our cryoET structures. AlphaFold prediction of individual
214 proteins returned low-confidence predictions for MC3, MC5, and MC15, but predicted that MC8
215 folds into a structure with a high-confidence pyramid-like domain formed by α helices (Fig. 4A),
216 which fits well into the MIP B8 density (Fig. 4B). To determine whether MC8 in fact corresponds
217 to the MIP B8 density, we performed cryoET on purified, demembranated flagella from control
218 and MC8 KD parasites (Fig. 4C-E). Because TMT analysis showed that MC8 is the only protein
219 lost in the MC8 KD (Supp. Fig. S3F; Supp. Dataset S1), any density altered in the knockdown
220 must correspond to MC8 itself. The subtomographic average of the 48-nm repeating unit from
221 MC8 KD axonemes was nearly identical to that of controls except for the absence of the MIP B8
222 density (Fig. 4C-E). Thus, MC8 is a bona fide, *T. brucei*-specific B-tubule MIP that is required for

223 normal parasite motility (Fig. 3C; Supp. Fig. S3B). The motility defect of MC8 KD parasites, in
224 which the only missing protein is MC8, demonstrates importance of lineage-specific MIPs to
225 flagellar motility.

226

227 **DISCUSSION**

228 **FAP106 knockdown provides insights into MIP assembly mechanisms.**

229 Functional analysis lags behind identification and structural assignment of MIP proteins. Here
230 we combine functional, structural, and proteomic analysis to demonstrate that the MIP FAP106
231 is required for motility and is a key interaction hub of the IJ and B-tubule MIP structures. The
232 role of FAP106 as a key interaction hub is emphasized by our finding that, while FAP106 is
233 required for stable assembly of FAP45 and lineage-specific MIP proteins MC3, 5, 8, and 15 (Fig.
234 2; Fig. 3, Fig. 5), loss of these individual proteins does not affect other MIP proteins or
235 structures (Supp. Fig. 3D-G; Fig. 4; Supp. Dataset S1; (19)). Thus, rather than interdependency,
236 our results suggest a hierarchical mechanism for B-tubule MIP assembly. FAP106-dependency
237 of FAP45 and a FAP210 structural homolog suggests that extensive interactions of FAP45 and
238 FAP210 with the tubulin lattice (13, 16) are relatively weak, while interactions with FAP106 (13)
239 are critical for stable binding and establishing their periodicity within the 48-nm repeat. This
240 supports the idea that an important role of MIPs is to enable complex assembly of proteins
241 along otherwise uniform protofilament polymers of tubulin (14) and suggests that loss of FAP45
242 and FAP210 in RIB72 mutants (34) may reflect dependency on FAP106 rather than a
243 requirement for RIB72 directly. Our studies also provide a structural explanation for motility
244 defects of FAP106 mutants in trypanosomes (Fig. 2), and in sperm from FAP106/ENKUR
245 mutants in mice (43).

246 **Holes in the IJ filament correspond to missing PACRG-B subunits, indicating**
247 **specialization of PACRG paralogs.**

248 PACRG alternates with FAP20 to form the highly conserved IJ filament (4, 5). One of the more
249 mysterious features of DMTs is a hole in the IJ filament that occurs once per 96-nm repeat in
250 most organisms and corresponds to a missing PACRG (8, 12, 37). *T. brucei* is unusual in
251 having two IJ holes per 96-nm repeat, one at the site of NDRC attachment as observed in other
252 organisms, and one proximal to the NDRC (15). The proximal hole is devoid of external
253 structures on the DMT (15), suggesting it is dictated by MIP interactions rather than NDRC
254 attachment, which is proposed for the NDRC hole (44). Our findings support this idea, as loss of
255 specific MIPs results in extra holes in the IJ filament. Some organisms have multiple PACRG
256 homologs (23, 38, 45), but the contribution of individual homologs is unknown. It is not known,
257 for example, if they are distinctly incorporated within a single axoneme or used for specialization
258 of axoneme function in different cell types or developmental stages. *T. brucei* has two PACRG
259 homologs, PACRG-A and PACRG-B, which have been suggested to be functionally redundant
260 (38, 39). Our structural and proteomics data instead support a model in which PACRG-A and
261 PACRG-B subunits both regularly assemble within each IJ filament, alternating with FAP20 in
262 turn, and with holes in the IJ filament corresponding to missing PACRG-B, but not PACRG-A
263 subunits (Fig. 2E). Distinct locations and assembly requirements for PACRG-A and PACRG-B
264 indicate they play distinct roles in assembly of the IJ. Although PACRG is conserved among
265 ciliated organisms, the family of PACRG proteins shows substantial heterogeneity in the N-
266 terminal region that has been shown to interact closely with the DMT lattice in *Chlamydomonas*
267 (21, 45). Divergent N-termini of PACRG-A versus PACRG-B may contribute to the differential
268 dependence on FAP106 and their distinct roles in assembly of the IJ.

269 **MC8 is a novel, lineage-specific T. brucei MIP that is required for normal parasite motility.**

270 The growing body of evidence suggests IJ subunits (PACRG and FAP20) and a core set of
271 conserved MIPs are found in all motile cilia, while other MIPs vary between organisms (13, 15,
272 16, 21, 23, 35, 37). FAP45, FAP52, and FAP106 represent core B-tubule MIPs while FAP126,
273 FAP276, and FAP210 are only found in some organisms (Table 1). We demonstrate that MC8 is
274 a bona fide lineage-specific MIP corresponding to the MIP B8 structure (Fig. 4). Loss of MC8 in
275 the FAP106 KD (Fig. 2B-2D) is likely due to loss of FAP45, which runs along protofilaments B7-
276 B8 (13, 16) and contacts FAP106 directly (13). Loss of MC8 compromises motility (Fig. 3C;
277 Supp. Fig. 3B) without affecting other MIPs (Fig. 4, Supp. Fig. 3F), demonstrating that lineage-
278 specific MIPs directly impact trypanosome motility. Validation of MC8 as a bona fide *T. brucei*
279 MIP in the current study, through a combination of mutant analysis, structural, functional, and
280 proximity proteomics approaches, demonstrates the power of this combined approach for MIP
281 identification and analysis. Our studies also strongly suggest that MC3, 5, and 15 likewise
282 correspond to novel, lineage-specific *T. brucei* MIPs. Trypanosome motility is necessary for
283 virulence in the mammalian host (32) and transmission through the tsetse fly vector (33).
284 Therefore, identification of novel, trypanosome-specific MIPs provides attractive targets to
285 consider for treatment of devastating diseases caused by these pathogens.

286 **Model for assembly of the IJ**

287 Our work provides an important advance toward elucidating the order of MIP assembly and
288 supports the following model for IJ assembly (Fig. 5). FAP20 binds every 8 nm, together with at
289 least a subset of PACRG, to form the IJ filament and this occurs independently from assembly
290 of FAP52 (21) and FAP106 (this work). FAP52 binds every 16 nm, independently of the IJ
291 filament (4) and FAP106 (this work), and may connect the IJ filament to the B-tubule via
292 FAP276 or other analogous structure (21, 35). FAP106 also binds every 16 nm, independently
293 from FAP52 (21), bridging the A- and B-tubules directly and serving as a critical guidepost for
294 assembling additional MIPs such as FAP45 and FAP210 (this work). Although FAP52 and

295 FAP106 bind regularly within each 48-nm repeat, their connections to other MIPs differ every 16
296 nm. Despite apparent contacts between FAP52 and other IJ MIPs (13, 16, 21, 35), assembly of
297 IJ MIPs in *Chlamydomonas* is largely unaffected by loss of FAP52 (21). Thus, while FAP52 and
298 FAP106 form contacts with each other and other IJ MIPs, they assemble independently from
299 one another, and FAP106 appears to be more critical for assembly of additional B-tubule MIPs.
300 Going forward, as additional MIPs are identified, particularly those that are lineage-specific,
301 application of combined proteomics, cryoEM, and mutant analysis, as done here, will be
302 necessary to completely define MIP assembly mechanisms and to yield a full understanding of
303 their contribution to flagellum function.

304

305 # MATERIALS AND METHODS

306 ***Trypanosoma brucei* culture**

307 Procyclic *T. brucei brucei* (strain 29-13) (46) were cultivated in SM medium (47) supplemented
308 with 10% heat-inactivated fetal bovine serum (FBS) at 28°C with 5% CO_2.

309 **In situ tagging**

310 mNeonGreen and APEX2-tagged cell lines were generated in the 29-13 background by C-
311 terminal tagging (40) with pPOTv6-puro-puro-mNG or pPOTv7-blast-blast-APEX2-3xHA,
312 respectively. pPOTv7-blast-blast-APEX2-3xHA contains the same APEX2-3xHA tag as in (48).
313 For MC3-NG, a transient CRISPR-Cas9 system (49) was used to tag both alleles. See Supp.
314 Table S2 for list of primers.

315 **Tetracycline-inducible knockdown**

316 Constructs for tetracycline-inducible knockdown were designed using RNAit (50) and cloned
317 into p2T7-177 (36). See Supp. Table S2 for list of primers. NotI-linearized plasmids were
318 transfected into 29-13 (FAP106 KD) or the corresponding MC-NG tagged cell lines (MC KDs)
319 using established methods (47). Clonal lines were generated by limiting dilution. Knockdown

320 was induced by growing cells in the presence of 1 µg/mL tetracycline (Tet) for at least 3d.
321 Control parasites were grown in the presence of tetracycline for comparison to the respective
322 KDs. For growth curves, cells were counted with a Beckman Coulter Z1 particle counter and
323 diluted daily to a concentration of 1e6 cells/mL, in triplicate.

324 **qRT-PCR**

325 Quantitative real-time PCR (qRT-PCR) was performed as previously described (51) with the
326 following modifications. FAP106-specific primers were designed using RNAit (50). Analyses
327 were performed in duplicate on three independent RNA preparations and values were
328 normalized to RPS23 (52). See Supp. Table S2 for list of primers.

329 **Motility analyses**

330 Cells were grown to ~1e6 cells/mL and loaded into polyglutamate-coated motility chambers (32)
331 sealed with Vaseline. 30s videos were acquired under dark-field illumination at ~40 frames per
332 second (fps) using a Hamamatsu ORCA-Flash 4.0 camera on a Zeiss Axio Imager A2 inverted
333 microscope with an EC Plan-Neofluar 10x/0.3 objective lens and Zen 2.6 Pro software. At least
334 five videos were collected for each independent biological replicate. Single cell tracking and
335 mean squared displacement were performed in MATLAB as previously described for fluorescent
336 parasites (32). For 'high density' motility analyses, cells were grown to ~1e7 cell/mL, then
337 diluted in conditioned medium to ~1e6 cells/mL and analyzed as above.

338 **Purification of demembranated flagella (detergent-extracted flagellum skeletons)**

339 Detergent extraction was done to demembranate flagellum skeletons, essentially as described
340 (15). Briefly, cells were washed in Dulbecco's PBS (DPBS), resuspended in Extraction buffer
341 (20 mM HEPES, pH 7.4, 1 mM $MgCl_2$, 150 mM NaCl, 0.5% NP40, 2x Sigmafast EDTA-free
342 protease inhibitor cocktail) for 15 min at room temperature, followed by depolymerization of
343 subpellicular microtubules with 1 mM $CaCl_2$ on ice for 30 min. Detergent-extracted flagellum
344 skeletons were pelleted at 1500 rcf for 10 min at 4°C.

345 **Flagellum length measurements**

346 For measurements of purified flagella, detergent-extracted flagellum skeletons were prepared
347 as described above and phase contrast images were acquired on a Zeiss Axioskop II
348 microscope with a Plan-Apochromat 63x/1.4 objective lens using Axiovision software. For
349 measurements of the paraflagellar rod (PFR) in detergent-extracted cytoskeletons, cells were
350 washed in Dulbecco's PBS (DPBS) and allowed to adhere to glass cover slips for 10 min. Cover
351 slips were rinsed to remove unattached cells, then extracted with PEME buffer (100 mM PIPES,
352 2 mM EGTA, 1 mM $MgSO_4$, 0.1 mM EDTA, pH 6.8) + 1% IGEPAL CA-630 (NP40) + 2x
353 Sigmafast EDTA-free protease inhibitor cocktail for 10 min. Cover slips were fixed in methanol
354 at -20°C for 10 min, allowed to dry, then rehydrated in DPBS for 15 min. Cover slips were
355 blocked in DPBS + 8% normal donkey serum + 2% bovine serum albumin then incubated in
356 rabbit anti-PFR2 (53) primary antibody diluted 1:1000 in blocking solution, followed by donkey
357 anti-rabbit Alexa 594 secondary antibody diluted 1:1500 in blocking solution. Cover slips were
358 mounted in Vectashield containing DAPI and images were acquired on a Zeiss Axioskop II
359 fluorescence microscope with a Plan-Apochromat 100x/1.4 objective lens and Axiovision or Zen
360 3.5 Pro software. Flagellum lengths were measured in Fiji using the freehand line tool and
361 analyzed in GraphPad Prism.

362 **CryoET**

363 CryoET grids and detergent-extracted flagellum skeletons were prepared essentially as
364 described (15). Briefly, 2e8 log phase cells were harvested and washed twice in DPBS.
365 Flagellum skeletons were prepared as described above, resuspended in 100 ul Extraction buffer
366 and spun over a 30% sucrose cushion in Extraction buffer without NP40 at 800 rcf for 5 min at
367 4°C. 100-150 µL of flagellum skeletons were collected from the upper fraction, washed once
368 with 700 ul Extraction buffer, and once with 1 mL Extraction buffer without NP40. Flagellum
369 skeletons were resuspended in Extraction buffer without NP40 and vitrified on quantifoil grids
370 with 5nm fiducial gold beads.

371 With *SerialEM* (54), tilt series were collected in a Titan Krios instrument equipped with a
372 Gatan imaging filter (GIF) and a post-GIF K3 direct electron detector in electron-counting mode
373 with parameters listed in Table S1. Frames in each movie of the raw tilt series were aligned,
374 drift-corrected, and averaged with *Motioncor2* (55). The micrographs in each tilt series were
375 aligned and reconstructed into 3D tomograms by either weighted back projections (WBP, for
376 sub-tomographic averaging) or simultaneous iterative reconstruction technique (SIRT, for
377 visualization and particle picking) using the *IMOD* software package (56). The contrast transfer
378 function (CTF) was determined by *ctffind4* (57) and corrected with the *ctfphaseflip* program (58)
379 of *IMOD*.

380 **Sub-tomogram averaging, visualization and modeling**

381 4x binned SIRT reconstructed tomograms were further processed by IsoNet (59) to improve the
382 contrast for particle picking. Because of their distinct features, radial spokes were picked as
383 particles to represent the centers of 96nm axonemal repeat units. These particles for 96 nm
384 repeat units were subject to three rounds of rough alignments with PEET (7, 60). The particle
385 coordinates for 48-nm repeat units were generated from the coordinates of the aligned particles
386 for 96-nm repeat units. While keeping all coordinates for 96-nm repeat units, extra coordinates
387 for 48-nm repeat units were added unidirectionally from the 96-nm-repeat-units coordinates in a
388 distance of 48nm along the axonemal axis. PEET alignments were performed on the particles of
389 48-nm repeat units to generate the final maps. In Summary, the sub-tomographic averages of
390 flagellar components from four datasets were generated from the following number of particles:
391 1014 particles from 20 tomograms of Control dataset 1, 728 particles from 18 tomograms of
392 FAP106 KD dataset, 1936 particles from 52 tomograms of MC8 KD dataset, and 538 particles
393 from nine tomograms of Control dataset 2. The cryoET sub-tomographic averaged maps have
394 been deposited in the Electron Microscopy Data Bank under the accession codes EMD-28802,
395 EMD-28803, EMD-28804, and EMD-28805, for FAP106 KD, Control 1, MC8 KD, and Control 2,

396 respectively. The resolution of each sub-tomographic average was calculated by
397 *calcUnbiasedFSC* in *PEET* based on the 0.143 FSC criterion (Supp. Fig. S2).
398 UCSF ChimeraX (61) was used to visualize reconstructed tomograms and sub-
399 tomographic averages. For surface rendering with UCSF ChimeraX, maps were first low pass
400 filtered to either 20Å or 30Å.
401 Model prediction of MC8 was performed by AlphaFold Colab (41, 42). AlphaFold
402 predicted model of MC8 was superimposed into our averaged density with the molmap and
403 fitmap functions in UCSF ChimeraX.
404 **TMT labeling and quantitative proteomics**
405 Detergent-extracted flagellum skeletons were prepared from 2e8-4e8 log phase cells as
406 described above. After detergent extraction and depolymerization of subpellicular microtubules,
407 the pellet of flagellum skeletons was washed in Extraction buffer without NP40 and solubilized in
408 100 µl 8M urea, 100 mM Tris, pH 8 for 15 min at room temperature. Samples were centrifuged
409 at full speed for 15 min to pellet any insoluble material. The supernatant was diluted with 100
410 mM Tris, pH 8 to a final concentration of 2M urea and precipitated with 20% ice-cold
411 trichloroacetic acid (TCA) on ice overnight. The sample was centrifuged at full speed for 30 min
412 at 4°C and washed twice with -20°C acetone. The TCA-precipitated pellets were dried and
413 stored at ≤-20°C.
414 *Sample Digestion:* Protein pellets were resuspended with digestion buffer (8M urea, 0.1M Tris-
415 HCl pH 8.5). Each sample was normalized by absorbance at 280 nm and 25µg was aliquoted
416 for the digestion. Samples were reduced and alkylated via sequential 20-minute incubations
417 with 5 mM TCEP and 10 mM iodoacetamide at room temperature in the dark. Carboxylate-
418 modified magnetic beads (CMMB) also known as SP3 (62) and ethanol (50% final
419 concentration) were added to each sample to induce protein binding to CMMB beads. CMMB
420 beads were washed three times with 80% ethanol and then resuspended with 18ul of 100 mM

421 TEAB. Protein samples were digested overnight with 1ul of 0.1µg/ul LysC (Promega) and 2ul of
422 0.4µg/ul trypsin (Pierce) at 37 °C.
423 *TMT Labeling and CIF Fractionation:* 9ul of 100% acetonitrile were added to each sample to a
424 final concentration of 30% (v/v). Then the TMT labels were resuspended with 100% acetonitrile.
425 25ug of each sample was labeled using TMT6plex (Thermo Fisher Scientific) and the four
426 labeled samples of each set (two independent biological replicates each of control and
427 knockdown) were pooled. The pooled samples were fractionated by CMMB-based Isopropanol
428 Gradient Peptide Fractionation (CIF) method (63) into six fractions before mass spectrometry
429 (MS) analysis.
430 *LC-MS Acquisition and Analysis:* Fractionated samples were separated on a 75uM ID x 25cm
431 C18 column packed with 1.9µm C18 particles (Dr. Maisch GmbH) using a 140-minute gradient
432 of increasing acetonitrile and eluted directly into a Thermo Orbitrap Fusion Lumos mass
433 spectrometer where MS spectra were acquired using SPS-MS3. Protein identification was
434 performed using MaxQuant (64) v 1.6.17.0. against a user assembled database consisting of all
435 protein entries from the TriTrypDB (65) for *T. brucei* strain 927 (version 7.0). Searches were
436 performed using a 20 ppm precursor ion tolerance. TMT6plex was set as a static modification
437 on lysine and peptide N terminal. Carbamidomethylation of cysteine was set as static
438 modification, while oxidation of methionine residues and N-terminal protein acetylation were set
439 as variable modifications. LysC and Trypsin were selected as enzyme specificity with maximum
440 of two missed cleavages allowed. 1% false discovery rate was used as a filter at both protein
441 and PSM levels. Statistical analysis was conducted with the MSstatsTMT Bioconductor package
442 (66). Raw proteomic data have been deposited to the Mass Spectrometry Interactive Virtual
443 Environment (MassIVE) under accession ID MSV000090661.
444

445 **ACKNOWLEDGMENTS**

446 We thank Daniel Velez-Ramirez for technical assistance with APEX2 proximity proteomics and
447 Simon Imhof for helpful discussions. We also thank Astra Bryant for assistance with high speed
448 microscopy and Jiayan Zhang for assistance with cryoET. Funding was provided by NIH grants
449 AI052348 (K.L.H.), GM071940 (Z.H.Z), and GM089778 (J.A.W). KJ was supported by the
450 Beckman Scholars Program (Beckman Foundation). We acknowledge the use of resources in
451 the Electron Imaging Center for Nanomachines supported by UCLA and grants from NIH
452 (S10RR23057 and S10OD018111) and NSF (DBI-1338135 and DMR-1548924).

453

454

455 # REFERENCES

456 1. J. Wallmeier *et al.*, Motile ciliopathies. *Nat Rev Dis Primers* **6**, 77 (2020).
457 2. T. Kruger, M. Engstler, Flagellar motility in eukaryotic human parasites. *Seminars in cell &*
458 *developmental biology* **46**, 113-127 (2015).
459 3. H. S. Judelson, F. A. Blanco, The spores of Phytophthora: weapons of the plant destroyer. *Nat*
460 *Rev Microbiol* **3**, 47-58 (2005).
461 4. E. E. Dymek *et al.*, PACRG and FAP20 form the inner junction of axonemal doublet microtubules
462 and regulate ciliary motility. *Mol Biol Cell* **30**, 1805-1816 (2019).
463 5. H. A. Yanagisawa *et al.*, FAP20 is an inner junction protein of doublet microtubules essential for
464 both the planar asymmetrical waveform and stability of flagella in Chlamydomonas. *Mol Biol Cell*
465 **25**, 1472-1483 (2014).
466 6. H. Sui, K. H. Downing, Molecular architecture of axonemal microtubule doublets revealed by
467 cryo-electron tomography. *Nature* **442**, 475-478 (2006).
468 7. D. Nicastro *et al.*, The molecular architecture of axonemes revealed by cryoelectron
469 tomography. *Science* **313**, 944-948 (2006).
470 8. D. Nicastro *et al.*, Cryo-electron tomography reveals conserved features of doublet microtubules
471 in flagella. *Proc. Natl. Acad. Sci. USA* **108**, E845-853 (2011).
472 9. M. Ichikawa *et al.*, Subnanometre-resolution structure of the doublet microtubule reveals new
473 classes of microtubule-associated proteins. *Nat Commun* **8**, 15035 (2017).
474 10. W. A. Anderson, R. A. Ellis, Ultrastructure of Trypanosoma Lewisi - Flagellum Microtublules and
475 Kinetoplast. *J Protozool* **12**, 483-& (1965).
476 11. K. Vickerman, On the surface coat and flagellar adhesion in trypanosomes. *J. Cell Sci.* **5**, 163-193.
477 (1969).
478 12. G. Pigino *et al.*, Comparative structural analysis of eukaryotic flagella and cilia from
479 Chlamydomonas, Tetrahymena, and sea urchins. *J Struct Biol* **178**, 199-206 (2012).
480 13. M. Gui *et al.*, De novo identification of mammalian ciliary motility proteins using cryo-EM. *Cell*
481 **184**, 5791-5806.e5719 (2021).
482 14. M. Ichikawa *et al.*, Tubulin lattice in cilia is in a stressed form regulated by microtubule inner
483 proteins. *Proc Natl Acad Sci U S A* **116**, 19930-19938 (2019).
484 15. S. Imhof *et al.*, Cryo electron tomography with volta phase plate reveals novel structural
485 foundations of the 96-nm axonemal repeat in the pathogen. *Elife* **8** (2019).
486 16. M. Ma *et al.*, Structure of the Decorated Ciliary Doublet Microtubule. *Cell* **179**, 909-922.e912
487 (2019).
488 17. P. Kiesel *et al.*, The molecular structure of mammalian primary cilia revealed by cryo-electron
489 tomography. *Nat Struct Mol Biol* **27**, 1115-1124 (2020).
490 18. S. Sun, R. L. Fisher, S. S. Bowser, B. T. Pentecost, H. Sui, Three-dimensional architecture of
491 epithelial primary cilia. *Proc Natl Acad Sci U S A* **116**, 9370-9379 (2019).
492 19. M. Owa *et al.*, Inner lumen proteins stabilize doublet microtubules in cilia and flagella. *Nat*
493 *Commun* **10**, 1143 (2019).
494 20. D. Stoddard *et al.*, Tetrahymena RIB72A and RIB72B are microtubule inner proteins in the ciliary
495 doublet microtubules. *Mol Biol Cell* **29**, 2566-2577 (2018).
496 21. A. A. Z. Khalifa *et al.*, The inner junction complex of the cilia is an interaction hub that involves
497 tubulin post-translational modifications. *Elife* **9** (2020).
498 22. T. Ide *et al.*, CFAP53 regulates mammalian cilia-type motility patterns through differential
499 localization and recruitment of axonemal dynein components. *PLoS Genet* **16**, e1009232 (2020).

500 23. S. Kubo *et al.*, Native doublet microtubules from Tetrahymena thermophila reveal the
501 importance of outer junction proteins. *bioRxiv* 10.1101/2022.09.30.510376,
502 2022.2009.2030.510376 (2022).
503 24. M. Rossi, G. Cicconofri, A. Beran, G. Noselli, A. DeSimone, Kinematics of flagellar swimming in
504 Euglena gracilis: Helical trajectories and flagellar shapes. *Proc Natl Acad Sci U S A* **114**, 13085-
505 13090 (2017).
506 25. J. L. Bargul *et al.*, Species-Specific Adaptations of Trypanosome Morphology and Motility to the
507 Mammalian Host. *PLoS Pathog* **12**, e1005448 (2016).
508 26. L. G. Wilson, L. M. Carter, S. E. Reece, High-speed holographic microscopy of malaria parasites
509 reveals ambidextrous flagellar waveforms. *Proc. Natl. Acad. Sci. USA* **110**, 18769-18774 (2013).
510 27. P. Buscher, G. Cecchi, V. Jamonneau, G. Priotto, Human African trypanosomiasis. *Lancet* **390**,
511 2397-2409 (2017).
512 28. K. I. Kasozi *et al.*, Prevalence of hemoprotozoan parasites in small ruminants along a human-
513 livestock-wildlife interface in western Uganda. *Vet Parasitol Reg Stud Reports* **17**, 100309 (2019).
514 29. L. Vincensini, T. Blisnick, P. Bastin, 1001 model organisms to study cilia and flagella. *Biol Cell* **103**,
515 109-130 (2011).
516 30. J. E. Donelson, M. J. Gardner, N. M. El-Sayed, More surprises from Kinetoplastida. *Proc. Natl.*
517 *Acad. Sci. USA* **96**, 2579-2581 (1999).
518 31. T. Kruger, S. Schuster, M. Engstler, Beyond Blood: African Trypanosomes on the Move. *Trends*
519 *Parasitol* **34**, 1056-1067 (2018).
520 32. M. M. Shimogawa *et al.*, Parasite motility is critical for virulence of African trypanosomes. *Sci*
521 *Rep* **8**, 9122 (2018).
522 33. B. Rotureau, C. P. Ooi, D. Huet, S. Perrot, P. Bastin, Forward motility is essential for trypanosome
523 infection in the tsetse fly. *Cell Microbiol* **16**, 425-433 (2014).
524 34. A. S. Fabritius *et al.*, Proteomic analysis of microtubule inner proteins (MIPs) in Rib72 null. *Mol*
525 *Biol Cell* **32**, br8 (2021).
526 35. S. Li, J. J. Fernandez, A. S. Fabritius, D. A. Agard, M. Winey, Electron cryo-tomography structure
527 of axonemal doublet microtubule from. *Life Sci Alliance* **5** (2022).
528 36. B. Wickstead, K. Ersfeld, K. Gull, Targeting of a tetracycline-inducible expression system to the
529 transcriptionally silent minichromosomes of Trypanosoma brucei. *Mol Biochem Parasitol* **125**,
530 211-216 (2002).
531 37. K. Song *et al.*, In situ structure determination at nanometer resolution using TYGRESS. *Nat*
532 *Methods* **17**, 201-208 (2020).
533 38. H. R. Dawe, H. Farr, N. Portman, M. K. Shaw, K. Gull, The Parkin co-regulated gene product,
534 PACRG, is an evolutionarily conserved axonemal protein that functions in outer-doublet
535 microtubule morphogenesis. *J. Cell Sci.* **118**, 5421-5430 (2005).
536 39. R. Broadhead *et al.*, Flagellar motility is required for the viability of the bloodstream
537 trypanosome. *Nature* **440**, 224-227 (2006).
538 40. S. Dean, J. D. Sunter, R. J. Wheeler, TrypTag.org: A Trypanosome Genome-wide Protein
539 Localisation Resource. *Trends Parasitol* **33**, 80-82 (2017).
540 41. J. Jumper *et al.*, Highly accurate protein structure prediction with AlphaFold. *Nature* **596**, 583-
541 589 (2021).
542 42. M. Mirdita *et al.*, ColabFold - Making protein folding accessible to all. *bioRxiv*
543 10.1101/2021.08.15.456425, 2021.2008.2015.456425 (2022).
544 43. M. K. Jungnickel *et al.*, The flagellar protein Enkurin is required for mouse sperm motility and for
545 transport through the female reproductive tract. *Biol Reprod* **99**, 789-797 (2018).
546 44. T. Heuser, M. Raytchev, J. Krell, M. E. Porter, D. Nicastro, The dynein regulatory complex is the
547 nexin link and a major regulatory node in cilia and flagella. *J. Cell Biol.* **187**, 921-933 (2009).

548 45. N. Khan *et al.*, Crystal structure of human PACRG in complex with MEIG1 reveals roles in
549 axoneme formation and tubulin binding. *Structure* **29**, 572-586 e576 (2021).
550 46. E. Wirtz, S. Leal, C. Ochatt, G. A. Cross, A tightly regulated inducible expression system for
551 conditional gene knock-outs and dominant-negative genetics in *Trypanosoma brucei*. *Mol.*
552 *Biochem. Parasitol.* **99**, 89-101 (1999).
553 47. M. Oberholzer, M. A. Lopez, K. S. Ralston, K. L. Hill, Approaches for functional analysis of flagellar
554 proteins in African trypanosomes. *Methods Cell Biol.* **93**, 21-57 (2009).
555 48. D. E. Velez-Ramirez *et al.*, APEX2 Proximity Proteomics Resolves Flagellum Subdomains and
556 Identifies Flagellum Tip-Specific Proteins in Trypanosoma brucei. *mSphere* **6** (2021).
557 49. S. Shaw, S. Knusel, S. Hoenner, I. Roditi, A transient CRISPR/Cas9 expression system for genome
558 editing in Trypanosoma brucei. *BMC Res Notes* **13**, 268 (2020).
559 50. S. Redmond, J. Vadivelu, M. C. Field, RNAit: an automated web-based tool for the selection of
560 RNAi targets in Trypanosoma brucei. *Mol. Biochem. Parasitol.* **128**, 115-118 (2003).
561 51. M. M. Shimogawa *et al.*, Cell Surface Proteomics Provides Insight into Stage-Specific Remodeling
562 of the Host-Parasite Interface in Trypanosoma brucei. *Mol Cell Proteomics* **14**, 1977-1988 (2015).
563 52. M. A. Lopez, E. A. Saada, K. L. Hill, Insect stage-specific adenylate cyclases regulate social motility
564 in african trypanosomes. *Euk Cell* **14**, 104-112 (2015).
565 53. E. A. Saada *et al.*, Insect stage-specific receptor adenylate cyclases are localized to distinct
566 subdomains of the Trypanosoma brucei Flagellar membrane. *Euk Cell* **13**, 1064-1076 (2014).
567 54. D. N. Mastronarde, Automated electron microscope tomography using robust prediction of
568 specimen movements. *J Struct Biol* **152**, 36-51 (2005).
569 55. X. Li *et al.*, Electron counting and beam-induced motion correction enable near-atomic-
570 resolution single-particle cryo-EM. *Nature methods* **10**, 584-590 (2013).
571 56. J. R. Kremer, D. N. Mastronarde, J. R. McIntosh, Computer visualization of three-dimensional
572 image data using IMOD. *J Struct Biol* **116**, 71-76 (1996).
573 57. A. Rohou, N. Grigorieff, CTFFIND4: Fast and accurate defocus estimation from electron
574 micrographs. *J Struct Biol* **192**, 216-221 (2015).
575 58. Q. Xiong, M. K. Morphew, C. L. Schwartz, A. H. Hoenger, D. N. Mastronarde, CTF determination
576 and correction for low dose tomographic tilt series. *J Struct Biol* **168**, 378-387 (2009).
577 59. Y.-T. Liu *et al.*, Isotropic Reconstruction of Electron Tomograms with Deep Learning. *bioRxiv*
578 10.1101/2021.07.17.452128, 2021.2007.2017.452128 (2021).
579 60. J. M. Heumann, A. Hoenger, D. N. Mastronarde, Clustering and variance maps for cryo-electron
580 tomography using wedge-masked differences. *J Struct Biol* **175**, 288-299 (2011).
581 61. T. D. Goddard *et al.*, UCSF ChimeraX: Meeting modern challenges in visualization and analysis.
582 *Protein Sci* **27**, 14-25 (2018).
583 62. C. S. Hughes *et al.*, Ultrasensitive proteome analysis using paramagnetic bead technology. *Mol*
584 *Syst Biol* **10**, 757 (2014).
585 63. W. Deng, J. Sha, K. Plath, J. A. Wohlschlegel, Carboxylate-Modified Magnetic Bead (CMMB)-
586 Based Isopropanol Gradient Peptide Fractionation (CIF) Enables Rapid and Robust Off-Line
587 Peptide Mixture Fractionation in Bottom-Up Proteomics. *Molecular & cellular proteomics : MCP*
588 **20**, 100039 (2021).
589 64. J. Cox, M. Mann, MaxQuant enables high peptide identification rates, individualized p.p.b.-range
590 mass accuracies and proteome-wide protein quantification. *Nat Biotechnol* **26**, 1367-1372
591 (2008).
592 65. M. Aslett *et al.*, TriTrypDB: a functional genomic resource for the Trypanosomatidae. *Nucleic*
593 *Acids Res.* **38**, D457-462 (2010).

594 66. T. Huang *et al.*, MSstatsTMT: Statistical Detection of Differentially Abundant Proteins in
595 Experiments with Isobaric Labeling and Multiple Mixtures. *Molecular & cellular proteomics :*
596 *MCP* **19**, 1706-1723 (2020).
597 67. J. Zhang *et al.*, Structure of the trypanosome paraflagellar rod and insights into non-planar
598 motility of eukaryotic cells. *Cell Discov* **7**, 51 (2021).

599

600

601 # FIGURE LEGENDS

602 **Figure 1. FAP106 is required for parasite motility.** 29-13 (Ctrl) and FAP106 knockdown
603 (FAP106 KD) parasites were grown in the presence of tetracycline to induce knockdown. (*A*)
604 qRT-PCR analysis of FAP106 mRNA levels. Graph shows the mean ± standard deviation from
605 three independent biological replicates. (*B*) Cumulative growth curve shows the mean cell
606 density vs time ± standard deviation from three independent biological replicates. (*C*) Histogram
607 shows the length distribution of purified, demembranated flagella. Inset shows a representative
608 phase contrast image. (*D*) Histogram shows the distribution of flagellum lengths as measured by
609 anti-paraflagellar rod (PFR) immunofluorescence microscopy in detergent-extracted
610 cytoskeletons. Inset shows a representative image of detergent-extracted cytoskeletons with
611 PFR in red. (*E*) Graph shows the mean ± standard deviation of flagellum lengths in *C* (Phase
612 Contrast) and *D* (anti-PFR). Phase contrast: Ctrl = 22.0 ± 2.5 μm, FAP106 KD = 19.0 ± 3.1 μm;
613 anti-PFR: Ctrl = 17.6 ± 2.7 μm, FAP106 KD = 14.2 ± 3.2 μm. N=50 flagella for each (*F*) Motility
614 tracks of individual parasites. (*G*) Mean squared displacement of parasites tracked in *F*. Dotted
615 lines indicate the upper and lower bounds of the standard error of the mean. Ctrl N=489;
616 FAP106 KD N=675. Data from an independent biological experiment are shown in Supp. Fig.
617 S1.

618 **Figure 2.** FAP106 is required for stable assembly of IJ MIPs and other MIP
619 structures. Demembranated flagella were purified from 29-13 (Ctrl) and FAP106 knockdown
620 (FAP106 KD) parasites grown in tetracycline to induce knockdown. Structure of the 48-nm
621 repeat of the DMT was obtained by cryoET, with subtomographic averaging. Densities are
622 colored according to the legend and based on similarity to published structures (13, 16, 21). (*A*)
623 Schematic illustrating a cross-section of the '9+2' axoneme and paraflagellar rod (PFR) viewed
624 from flagellum tip to base. Adapted from (67). Enlarged panel shows a single DMT, with A- and
625 B-tubules indicated (A_t, B_t) and protofilaments numbered. FAP106 (red) and the inner junction

626 filament (IJ) comprised of alternating PACRG (blue) and FAP20 (purple) are colored for
627 reference. Viewing angles shown in *C-E* are indicated. (*B*) Cross-sectional view of the DMT.
628 Colored densities indicate structures reduced or missing in FAP106 KD compared to Ctrl. (*C*
629 and *D*) Longitudinal views of the DMT. Viewing angles are indicated in *A, inset*. The 48-nm
630 repeat is indicated. Note that *T. brucei* has a structure similar to FAP210 of *Chlamydmonas*
631 (green) despite not having a clear FAP210 homolog (Table 1). (*E*) Longitudinal views of the
632 DMT, showing the IJ filament. Viewing angles are indicated in *A, inset.* The 48-nm repeat is
633 indicated. Black arrowheads indicate the position of the single hole found within each 48-nm
634 repeat in Ctrl DMTs. FAP20 and PACRG subunits are colored according to the legend, with
635 holes corresponding to missing PACRG-B subunits, as suggested by TMT proteomics (Figure
636 3).

637 **Figure 3. TMT proteomics identifies novel, lineage-specific MIP candidates.** (*A*)
638 Demembranated flagella were purified from 29-13 (Ctrl) or FAP106 KD parasites grown in
639 tetracycline to induce knockdown. Volcano plot shows significance (-Log_{10} Adjusted P-value) vs.
640 relative abundance (Log_2 Fold-Change) for all proteins quantified by TMT proteomics. Relative
641 abundance is calculated as FAP106 KD/Ctrl. Results are from two independent biological
642 samples. Proteins that met the filtering criteria (2-fold decrease, adjusted P-value $\leq$0.06; Table
643 2; Supp. Dataset S1) are indicated by red dots. Labels indicate known proteins (red text) and
644 putative MIP candidates (green text). Asterisks indicate proteins that were independently
645 identified as putative B-tubule MIP candidates in a separate proximity labeling approach (Supp.
646 Fig. S3; Supp. Dataset S2). (*B*) Cross-sectional view of the DMT as viewed from the flagellum
647 tip, showing the positions of MIP structures lost in FAP106 KD as observed by cryoET (Fig. 2),
648 with known MIPs colored. A- and B-tubules are indicated (A_t, B_t) and protofilaments are
649 numbered. (*C*) Motility analysis showing mean squared displacement of 29-13 (Ctrl) and MC KD
650 parasites from $\geq$2 independent biological replicates. Dotted lines indicate the upper and lower

651 bounds of the standard error of the mean. Ctrl N=1761; MC3 KD N=627; MC5 KD N=753; MC8
652 KD N=709, MC15 KD N=751. Individual replicates are shown in Supp. Fig. S3B. (*D*) Detergent-
653 extracted cytoskeletons were prepared from the indicated KD parasites or their respective
654 mNeonGreen (NG)-tagged parental cell lines (Ctrl). Graph shows the mean ± standard
655 deviation of flagellum lengths as measured by anti-PFR immunofluorescence microscopy. MC3-
656 NG (Ctrl) = 19.9 ± 2.3 µm, MC3 KD = 19.3 ± 1.8 µm; MC5-NG (Ctrl) = 18.9 ± 2.4 µm, MC5 KD =
657 19.1 ± 2.3 µm; MC8-NG (Ctrl) = 19.6 ± 2.9 µm, MC8 KD = 18.0 ± 2.5 µm, MC15-NG (Ctrl) =
658 18.4 ± 2.1 µm, MC15 KD = 16.7 ± 2.6 µm. N=50 flagella for each, except N=45 flagella for
659 MC15-NG.

660 **Figure 4. MC8 is a novel, lineage-specific *T. brucei* MIP that comprises the MIP B8**
661 **density.** (*A*) AlphaFold prediction for MC8 (41, 42), colored according to confidence. Box
662 indicates high-confidence region modeled in *B*. (*B*) MC8 AlphaFold prediction modeled into MIP
663 B8 cryoET density. (*Left*) Cross-sectional view of the DMT, with the MIP B8 density colored
664 aqua. (*Middle, Right*) Enlarged view of MIP B8 density with AlphaFold prediction shown in aqua.
665 Viewing angle shown in *Right* panel is indicated by the dashed line in *Middle* panel. (*C-E*)
666 Demembranated flagella were purified from 29-13 (Ctrl) and MC8 knockdown (MC8 KD)
667 parasites grown in tetracycline to induce knockdown. Structure of the 48-nm repeat of the DMT
668 was obtained by cryoET, followed by subtomographic averaging. (*C*) Cross-sectional view of the
669 DMT with MIP B8 density colored in aqua. (*D* and *E*) Longitudinal views of the DMT. Viewing
670 angles and colors are as indicated in Fig. 2.

671 **Figure 5. FAP106 is required for motility and stable assembly of conserved and lineage-**
672 **specific MIPs at the inner junction.** Normal parasite motility relies on FAP106 as a critical
673 interaction hub for assembly of MIPs at the inner junction (IJ). Cross-sectional and longitudinal
674 views of the DMT are illustrated. Conserved IJ MIPs PACRG-A, FAP20 and FAP52 assemble
675 independently of FAP106, however PACRG-B does not stably assemble into the IJ filament

676 without FAP106. The B-tubule remains intact and connected to the A-tubule at the IJ, despite
677 loss of multiple IJ MIPs. FAP106 is also critical for stable assembly of the conserved MIP,
678 FAP45, and a FAP210-like protein (modeled as filaments based on published structures (13, 16,
679 21)), as well as several novel, lineage-specific MIPs.

Table 1. Known B-tubule MIPs

Chlamydomonas	**Mammals**	***Tetrahymena***	***Trypanosoma***
†PACRG	PACRG	TTHERM_00446290; TTHERM_00499310; TTHERM_00499570	Tb927.3.2310; Tb927.9.9940
†FAP20	CFAP20	TTHERM_00418580	Tb927.10.2190
FAP45	CFAP45	TTHERM_001164064	Tb927.8.4580
FAP52	CFAP52	TTHERM_01094880	Tb927.11.7560
FAP106	ENKUR	TTHERM_00137550; TTHERM_00370750	Tb927.11.4880
FAP210	CFAP210	TTHERM_00643530	*
FAP126	Flattop		
FAP276	CFAP276		
FAP90			
FAP112			
	EFCAB6		
			Tb927.11.2770 (MIP B8, this study,‡)

*Possible analogous structure present, but no clear sequence homolog

†FAP20 and PACRG form the IJ filament

‡Corresponding structure was called 'MIP3c' in (15) but our current study suggests this structure is distinct from MIP3c (FAP45).

Table 2. Proteins significantly reduced in FAP106 KD flagellum skeletons by TMT proteomics

Gene	Gene ID	Fold Reduction	Adjusted P-value	Protein Localization	Function
FAP106	Tb927.11.4880	24.02	0.0011	Flagellum	B-tubule MIP
FAP45	Tb927.8.4580	3.95	0.0035	Flagellum	B-tubule MIP
PACRG-B	Tb927.9.9940	2.77	0.0576	Flagellum	IJ filament
MC5	Tb927.11.4920	13.74	0.0003	Flagellum	MIP candidate*
MC3	Tb927.10.7120	3.44	0.0044	Flagellum	MIP candidate*
MC8	Tb927.11.2770	2.81	0.0111	Flagellum	MIP candidate*
MC15	Tb927.3.3200	1.95	0.0177	Flagellum	MIP candidate*
RPC19	Tb927.11.8890	2.99	0.0055	Nucleus	RNA polymerase

*Identified by independent APEX2-based proximity proteomics of known B-tubule MIPs (see Supp. Dataset S2)

Figure 1

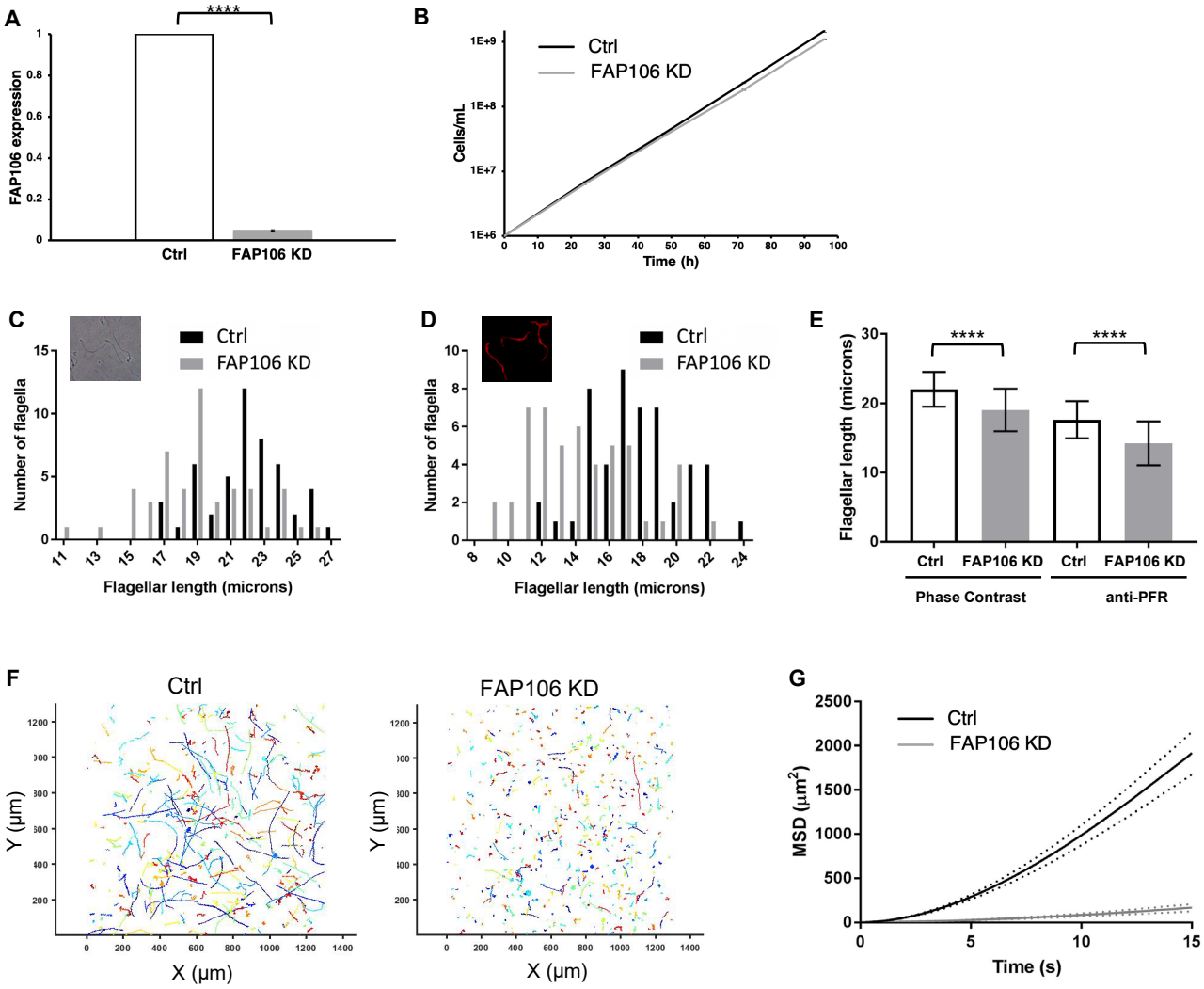
A
****
FAP106 expression
Ctrl
FAP106 KD
B
Ctrl
FAP106 KD
Cells/mL
Time (h)
C
Ctrl
FAP106 KD
Number of flagella
Flagellar length (microns)
D
Ctrl
FAP106 KD
Number of flagella
Flagellar length (microns)
E
****
****
Flagellar length (microns)
Ctrl
FAP106 KD
Ctrl
FAP106 KD
Phase Contrast
anti-PFR
F
Ctrl
FAP106 KD
Y (µm)
X (µm)
G
Ctrl
FAP106 KD
MSD (µm²)
Time (s)

Figure 2

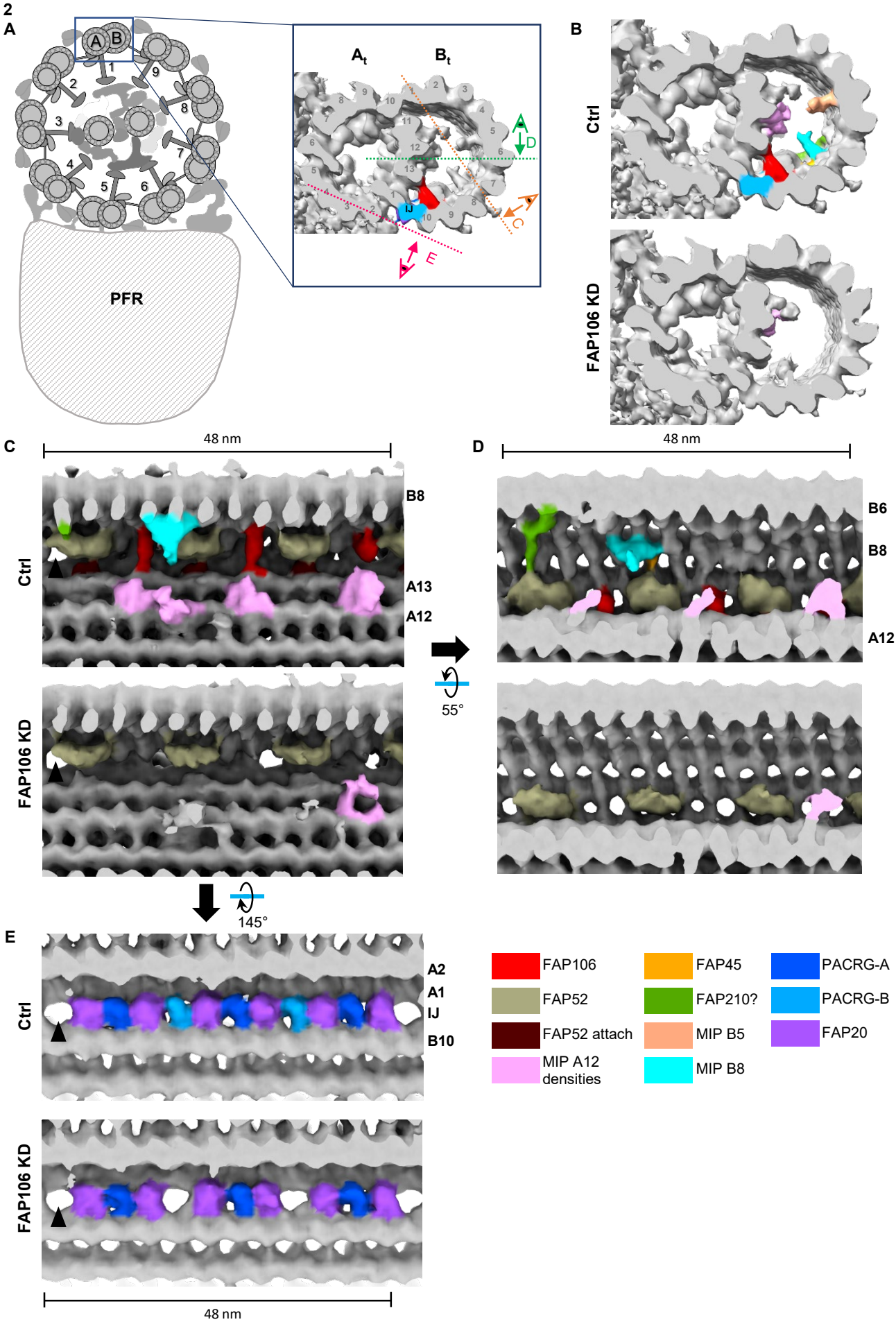
A
A
B
1
2
3
4
5
6
7
8
9
PFR
A_t
B_t
IJ
D
C
E
B
Ctrl
FAP106 KD
C
48 nm
Ctrl
B8
A13
A12
FAP106 KD
55°
D
48 nm
B6
B8
A12
145°
E
Ctrl
A2
A1
IJ
B10
FAP106 KD
48 nm
FAP106
FAP52
FAP52 attach
MIP A12 densities
FAP45
FAP210?
MIP B5
MIP B8
PACRG-A
PACRG-B
FAP20

Figure 3

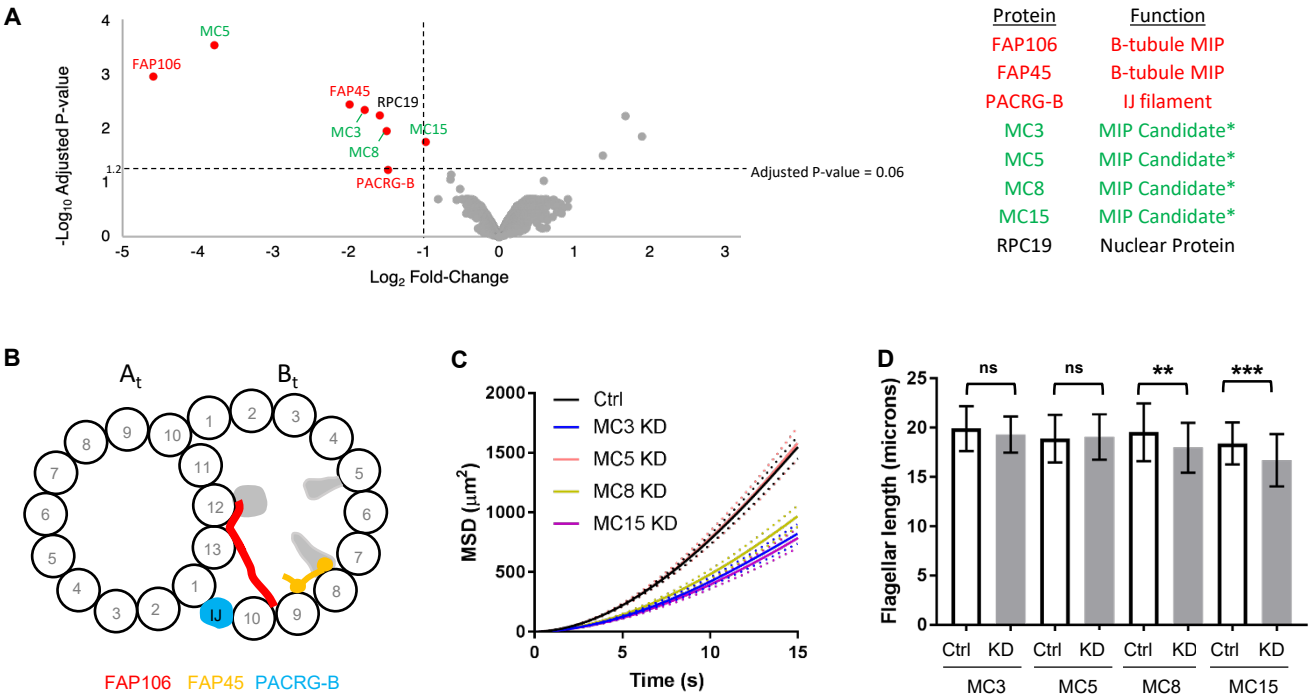
A
MC5
FAP106
FAP45
RPC19
MC3
MC15
MC8
PACRG-B
1.2
Adjusted P-value = 0.06
-Log10 Adjusted P-value
Log2 Fold-Change
Protein
Function
FAP106
B-tubule MIP
FAP45
B-tubule MIP
PACRG-B
IJ filament
MC3
MIP Candidate*
MC5
MIP Candidate*
MC8
MIP Candidate*
MC15
MIP Candidate*
RPC19
Nuclear Protein
B
At
Bt
IJ
FAP106
FAP45
PACRG-B
C
Ctrl
MC3 KD
MC5 KD
MC8 KD
MC15 KD
MSD (μm2)
Time (s)
D
ns
ns
**
***
Flagellar length (microns)
Ctrl
KD
MC3
MC5
MC8
MC15

Figure 4

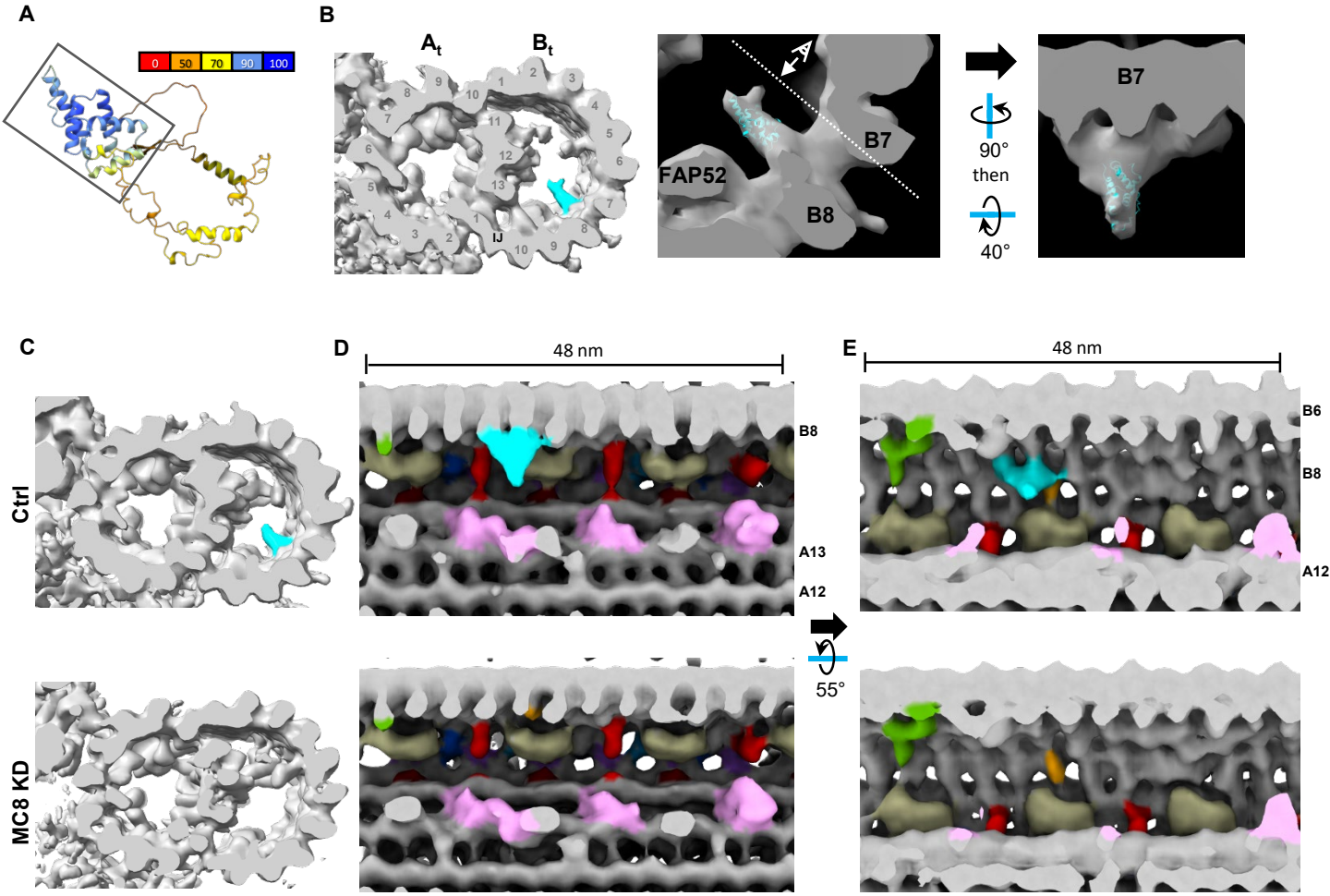
A
0
50
70
90
100
B
A_t
B_t
IJ
FAP52
B7
B8
90°
then
40°
C
Ctrl
MC8 KD
D
48 nm
B8
A13
A12
55°
E
48 nm
B6
B8
A12

Figure 5

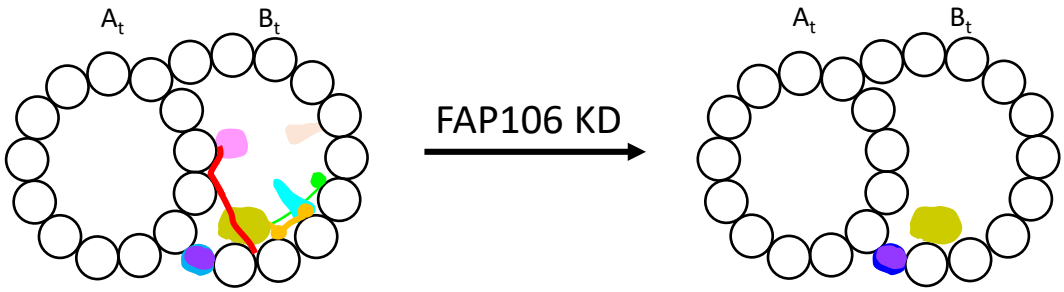

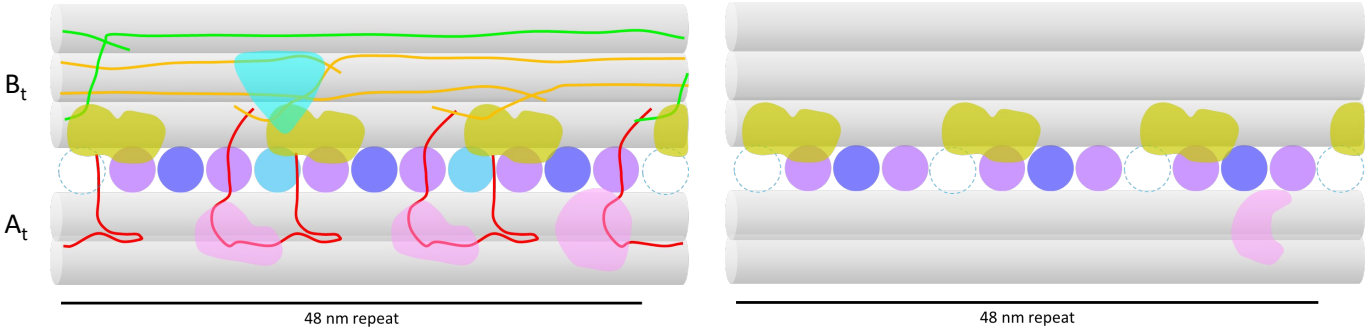

FAP20
PACRG-A
PACRG-B
} IJ filament
FAP45
FAP52
FAP106
MIP B8
FAP210-like
MIP A12
MIP B5
} Lineage-specific MCs

FAP20
PACRG-A
PACRG-B
} IJ filament
FAP45
FAP52
FAP106
MIP B8
FAP210-like
MIP A12
MIP B5
} Lineage-specific MCs